materials

MDPI

Article

Charge Trapping and Emission Properties in CAAC-IGZO Transistor: A First-Principles Calculations

Ziqi Wang [1,2,3], Nianduan Lu [1,2,3,*], Jiawei Wang [1,2,3], Di Geng [1,2,3], Lingfei Wang [1,2,3] and Guanhua Yang [1,2,3]

[1] State Key Lab of Fabrication Technologies for Integrated Circuits, Institute of Microelectronics, Chinese Academy of Sciences, Beijing 100029, China; wangziqi@ime.ac.cn (Z.W.)
[2] Laboratory of Microelectronic Devices and Integrated Technology, Institute of Microelectronics, Chinese Academy of Sciences, Beijing 100029, China
[3] University of Chinese Academy of Sciences, Beijing 100029, China
* Correspondence: lunianduan@ime.ac.cn

Abstract: The c-axis aligned crystalline indium-gallium-zinc-oxide field-effect transistor (CAAC-IGZO FET), exhibiting an extremely low off-state leakage current (~10^{-22} A/μm), has promised to be an ideal candidate for Dynamic Random Access Memory (DRAM) applications. However, the instabilities leaded by the drift of the threshold voltage in various stress seriously affect the device application. To better develop high performance CAAC-IGZO FET for DRAM applications, it's essential to uncover the deep physical process of charge transport mechanism in CAAC-IGZO FET. In this work, by combining the first-principles calculations and nonradiative multiphonon theory, the charge trapping and emission properties in CAAC-IGZO FET have been systematically investigated. It is found that under positive bias stress, hydrogen interstitial in Al_2O_3 gate dielectric is probable effective electron trap center, which has the transition level (ε (+1/−1) = 0.52 eV) above Fermi level. But it has a high capture barrier about 1.4 eV and low capture rate. Under negative bias stress, oxygen vacancy in Al_2O_3 gate dielectric and CAAC-IGZO active layer are probable effective electron emission centers whose transition level ε (+2/0) distributed at −0.73~−0.98 eV and 0.69 eV below Fermi level. They have a relatively low emission barrier of about 0.5 eV and 0.25 eV and high emission rate. To overcome the instability in CAAC-IGZO FET, some approaches can be taken to control the hydrogen concentration in Al_2O_3 dielectric layer and the concentration of the oxygen vacancy. This work can help to understand the mechanisms of instability of CAAC-IGZO transistor caused by the charge capture/emission process.

Keywords: carrier capture and emission; c-axis aligned crystalline indium-gallium-zinc-oxide (CAAC-IGZO); first principles calculation; transistor instability effect

Citation: Wang, Z.; Lu, N.; Wang, J.; Geng, D.; Wang, L.; Yang, G. Charge Trapping and Emission Properties in CAAC-IGZO Transistor: A First-Principles Calculations. *Materials* **2023**, *16*, 2282. https://doi.org/10.3390/ma16062282

Academic Editor: Jeonghun Kwak

Received: 28 February 2023
Revised: 8 March 2023
Accepted: 9 March 2023
Published: 12 March 2023

1. Introduction

Benefited from the high mobility and good large-area uniformity, indium-gallium-zinc-oxide (IGZO) has received a lot of attention since it was discovered in 2004 [1]. After years of development, this material is making its entry into the display industry, thanks to its better performance than amorphous silicon [2–5]. Recently, a new crystalline oxide semiconductor called c-axis aligned crystalline IGZO (CAAC-IGZO) has also caught the attention of researchers. Field-effect transistors (FETs) with the CAAC-IGZO channel layer exhibit an extremely low off-state leakage current (~10^{-22} A/μm) [6,7], which helps to further reduce the leakage power in-memory application. More importantly, the mobility of the CAAC-IGZO FET doesn't degrade at high temperatures [8]. In terms of the potential advantages of extremely low power, high mobility, capacitorless architecture and back-end-of-line (BEOL) compatibility [9–11], the CAAC-IGZO FET has promised to be an ideal candidate for DRAM applications [7,12,13].

Despite its benefits, the instability of CAAC-IGZO FETs greatly limits their application. These instabilities are mainly reflected in the drift of the threshold voltage when the device works continuously in various stress, which are usually distinguished: negative bias stress (NBS) and positive-bias stress (PBS). That is, NBS instabilities shift the transfer curve of the FET negatively, while PBS shifts it positively. To clearly explain the fundamental performance of IGZO transistors, a great deal of possible mechanisms have been proposed [14–19], for instance, charge trapping processes at the interfaces and/or in the dielectric, the creation and impact of deep traps in active layer, the absorption of oxygen or water molecules at the channel interface, the removal of oxygen interstitials, the capture of electrons by oxygen vacancies, the reduction of peroxide concentration, and the desorption and diffusion of hydrogen, and so on. However, due to the complexity of the dielectric layer and semiconductor layer, the origin of the bias instabilities in CAAC-IGZO FETs is still controversial. On the other hand, thanks to the sensitivity of the transistors to various factors, such as the deposition conditions, annealing conditions and gate-dielectric material, it is difficult to isolate the impact of different origins on reliability. Therefore, to better develop high-performance CAAC-IGZO FETs for DRAM applications, it's essential to uncover the deep physical process of charge transport mechanisms in CAAC-IGZO FETs.

In this work, we systematically investigate the charge trapping and emission properties in CAAC-IGZO FETs based on a first-principles calculations. Then, by combining the nonradiative multiphonon theory, the trapping process properties of several intrinsic defects in CAAC-IGZO stack with Al_2O_3 dielectric have been discussed in detail. Finally, the influence of charge trapping process on the reliability of devices has also been discussed under positive bias stress (PBS) and negative bias stress (NBS).

2. Computation Methodology

To uncover the charge trapping and emission properties, a general FET is selected as a prototype device. Figure 1 shows the illustration of the carrier trapping process in CAAC-IGZO FET with active layer of CAAC-IGZO and gate dielectric of Al_2O_3. The first-principles calculations were utilized based on the density functional theory (DFT) of the first-principle plane-wave pseudopotential method. All calculations were performed by the Vienna Ab Initio Simulation Package (VASP) software [20]. The projector augmented wave (PAW) [21] pseudopotential was used to describe the interactions between the nucleus and valence electrons. The generalized gradient approximation (GGA) with the Perdew-Burke-Ernzerhof (PBE) functional was selected to model the exchange and correlation interactions [22]. The cut-off energy for the wave function was set to 500 eV. All structural models were fully relaxed using the conjugate gradient algorithm until the atomic force was less than 0.01 eV/Å.

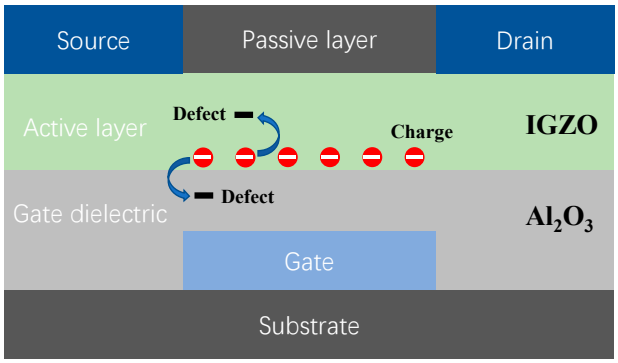

Figure 1. Illustration of carrier trapping process in CAAC-IGZO FET.

The hybrid functional of Heyd-Scuseria-Ernzerhof (HSE06) was used to ensure the accuracy of bandgap calculation and avoid the small bandgap under GGA-PBE function [23]. 30% and 15% of PBE were replaced with Hartree-Fock function in the calculation of Al_2O_3 and IGZO, respectively. To avoid overestimation of metal *d* bands, the GGA+*U* method was used to include an on-site Coulomb correlation interaction between the localized metal *d* electrons [24]. The parameters of U = 8.0 eV, 8.0 eV, 8.0 eV and under PBE function and U = 3.5 eV, 4.0 eV, 4.0 eV under HSE06 function were selected for In 3*d*, Ga 3*d* and Zn 3*d* orbitals, respectively.

Figure 2 shows the crystal model of α-Al_2O_3 and CAAC-IGZO. Al_2O_3 as a gate dielectric is often grown by ALD to form an amorphous structure. However, Choi et al. [25] confirmed that the features of native defect in Al_2O_3 are not strongly dependent on the phase, and the results in the α-Al_2O_3 are representative and applicable to an amorphous structure. The optimized lattice parameters for the perfect α-Al_2O_3 crystal are $a = b$ = 4.767 Å and c = 13.028 Å, which are good agreement with the experimental values with $a = b$ = 4.656 Å and c = 13.140 Å [26]. To simulate the defects, a supercell of 2 × 2 × 1 with 120 atoms was used. The optimized lattice parameters for the perfect CAAC-IGZO crystal are $a = b$ = 3.345 Å and c = 26.083 Å, which are good agreement with the experimental values with $a = b$ = 3.2948 Å [27] and c = 26.071 Å [28]. To reduce the interaction of defects in the *a-b* plane, a supercell with 112 atoms was used. The supercell was obtained by setting lattice vectors to (420), (040), and (221) for the IGZO crystal and reducing the lattice constant c to one-third [29]. To have an insight into the capture process of the CAAC-IGZO FETs with Al_2O_3 dielectric, a variety of different intrinsic defects are considered, which may widely exist and have been suggested as the cause of reliability issues [30–35] in oxide semiconductor materials, for instance, oxygen vacancy (V_O), oxygen interstitial (O_i), hydrogen interstitial (H_i), hydrogen substituted oxygen (H_O) and hydroxyl interstitial ($(OH)_i$), and so on. Here, the defect of Ho can be regarded as a coexistence of H_i and V_O. And the defect of $(OH)_i$ can be regarded as a coexistence of H_i and O_i. In IGZO crystalline, because of the different chemical environment from nearby metal atoms, four kinds of oxygen vacancy will be created by removing the selected oxygen atoms, as well as two kinds of oxygen interstitial, as shown in Figure 2b.

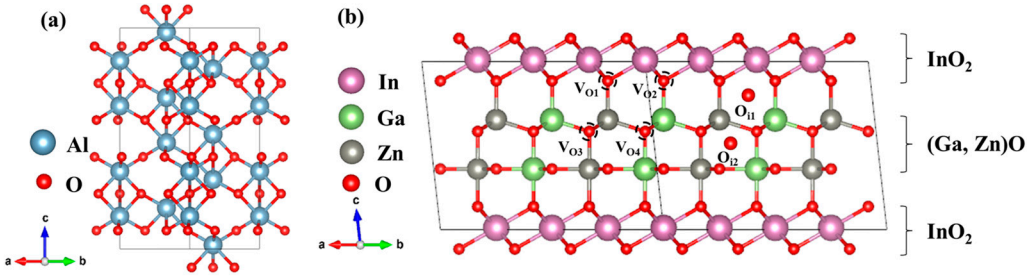

Figure 2. Crystal structure of (**a**) α-Al_2O_3 and (**b**) CAAC-IGZO. The structural model is drawn with VESTA [36].

3. Result and Discussion

3.1. Formation Energy and Transition Level

As mentioned above, the CAAC-IGZO FETs may be affected by a variety of defects. To identify which defects have an impact on the FET, the formation energy of all kinds of defects will be discussed firstly. The formation energy of defect can be obtained as [37],

$$E_{for}^{q} = E_{defect}^{q} - E_{perfect} - \sum_i n_i \mu_i + q(E_f + E_v + \Delta V), \quad (1)$$

where E_{defect}^{q} represents the total energy of a supercell with the defect in the cell, $E_{perfect}$ is the total energy for a perfect supercell, n_i is the number of atoms removed from or added to the supercell to form a defect, μ_i is the chemical potentials of oxygen and

hydrogen atom/ion, q represents the number of electrons transferred from or to electron reservoirs [38,39], E_f refers to the Fermi level relative to the valence band maximum energy (VBM, E_v) position in a perfect supercell. The correction term, ΔV, is referred to as the electrostatic potential that is far from the defect in the supercell with respect to the perfect supercell of the same size. Otherwise, in order to determine the position of the defect level in the band gap, one can calculate the transition level. Based on Equation (1), the position of the Fermi level at which the formation energy of charge states q equals to the formation energy of charge states q' was defined as transition level $\varepsilon(q/q')$ [37].

Generally, by using the charged formation energy and transition level, one can clearly understand the stability of defect and the relative position of defect level in the bandgap from an energy perspective. Figure 3 shows the formation energy of each defect under O-rich conditions In this work, the Fermi level of IGZO channel is set at 0.2 eV below E_C in the absence of an electric field, which is a reasonable assumption [2,40]. From in Figure 3a, as compared with the other oxygen vacancies in IGZO, V_{O1}, being nearby an In atom and Zn atom, exhibits the lowest formation energy. This result indicates that V_{O1} may exist more stably in IGZO than other oxygen vacancies, which is attributed to the weak bonding between In atom and O atom. It is noting that unlike the role of oxygen vacancies in a-IGZO and some transition metal oxides [31,41], oxygen holes do not act as n-type electron donors in CAAC-IGZO. In contrast, the formation energy of interstitial oxygen does not depend significantly on the metal ions in its vicinity. More importantly, our calculations also show the most stable charge states for each intrinsic defect in IGZO and Al_2O_3 without an electric field. In the absence of electric field, the Fermi level is 0.2 eV below E_C and the most stable charge states for intrinsic defects (V_O, O_i, H_i, H_O and $(OH)_i$) in IGZO, are 0, −2, +1, +1 and −1, respectively. And the most stable charge states for intrinsic defects (V_O, O_i, H_i, H_O, and $(OH)_i$) in Al_2O_3, are also 0, −2, +1, +1 and −1, respectively. These charged defects will form a charged center in oxide and lead to the fixed oxide charge, and then significantly influence the electrical characteristics of transistor. As a result, H_i and H_O defects will lead to positive fixed oxide charge, while O_i and $(OH)_i$ will result in a negative fixed oxide charge.

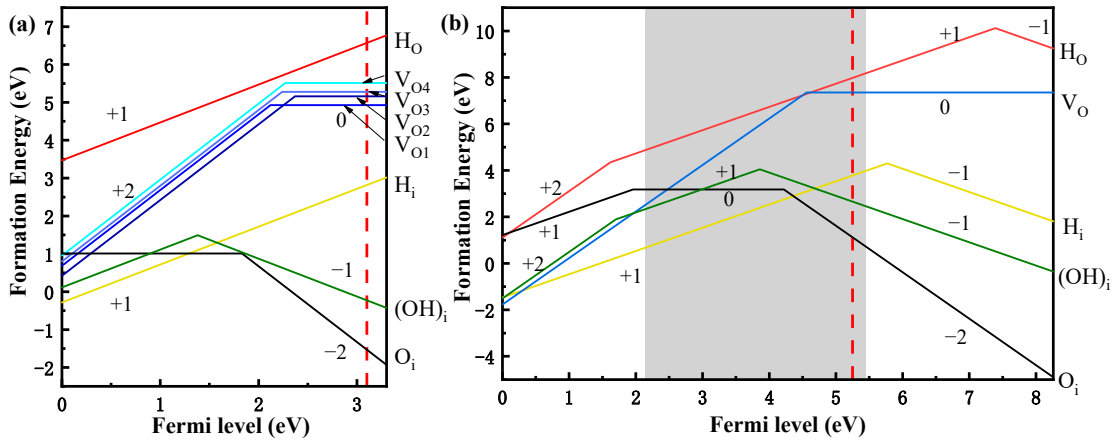

Figure 3. The formation energy of defects under O-rich condition for CAAC-IGZO (**a**) and Al_2O_3 (**b**). The red dotted line represents the Fermi level in the absence of an electric field and the grey area in (**b**) represents the area of band gap in CAAC-IGZO.

Figure 4 shows the band alignment and transition level of defects in Al_2O_3/IGZO system. In general, the transition levels reveal which defects undergo electron capture or emission. With the position of the Fermi level changes in the presence of electric field, the defects will capture electrons when the Fermi level is higher than the transition level as well as emission electrons when the Fermi level is lower than the transition level. Therefore, if the transition level is closer to the Fermi level, the defect is a more efficient center

for electron capture or emission under the electric field. In Figure 4, one can see that the transition level ε (+1/−1) of H_i in Al_2O_3 is 0.52 eV above the Fermi level of CAAC-IGZO which is closer to the Fermi level, as compared with the transition level ε (+1/−1) of H_O in Al_2O_3 which is 2.14 eV above Fermi level. This result suggests that the defect H_i in Al_2O_3 gate dielectric is probable effective electron trap center for CAAC-IGZO channel under PBS. The reason is that when a positive bias voltage is applied, the bandgap of the gate dielectric is shifted downwards, thus allowing the process of electron capture more likely to occur in H_i defects in Al_2O_3 gate dielectric. The detailed schematics for electron trapping process under PBS can be seen in Figure 5a. In contrary, the transition levels ε (+2/0) of Vo in CAAC-IGZO and ε (+2/0) of Vo in Al_2O_3 are distributed at −0.73~−0.98 eV and 0.69 eV below the Fermi level of CAAC-IGZO, respectively. The transition level ε (+2/0) for Vo in CAAC-IGZO and Al_2O_3 is closer to the Fermi level, as compared with other defects. The results indicate that the oxygen vacancies in CAAC-IGZO active layer and Al_2O_3 gate dielectric are likely to be the electron emission center under NBS, due to the bandgap of gate dielectric shifting upwards thus allowing the process of electron emission. Figure 5b shows the schematics of electron emission process under NBS in detailed. The properties of electron capture or release in these defects will be discussed in more detail in the following.

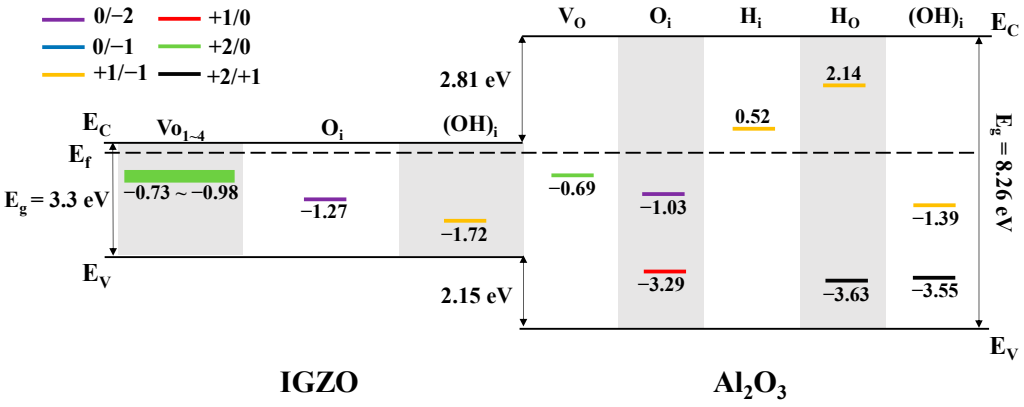

Figure 4. The band alignment and charged transition level of defects in Al_2O_3/IGZO. The numbers in the figure represent the energy from the transition level to the Fermi level of CAAC-IGZO.

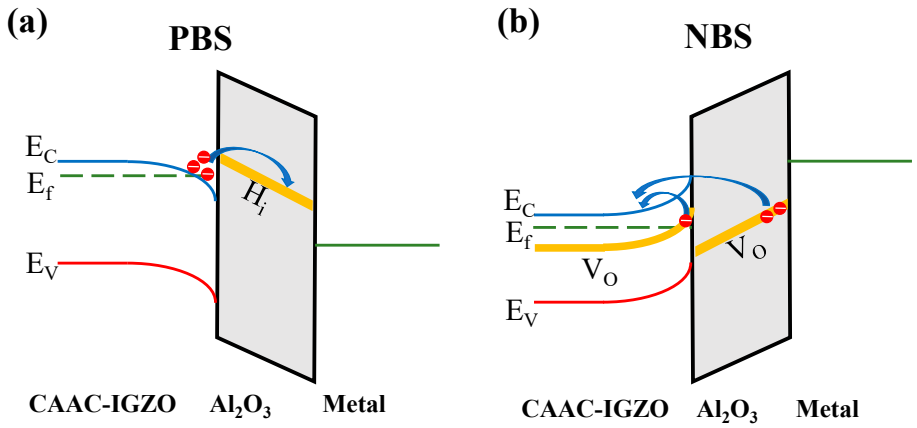

Figure 5. The schematics diagram of electron trapping process under PBS (**a**), and the electron emission process under NBS (**b**). Electrons are exchanged between the intrinsic defects and the conduction band of the CAAC-IGZO. Under PBS, electrons will be trapped in H_i defects in Al_2O_3. Under NBS, electrons will be emitted from Vo defect in CAAC-IGZO and Al_2O_3.

3.2. Electronic Properties of Charge Capture/Emission Process

According to the analysis of the transition levels above, one can determine that H_i in Al_2O_3 is the possible electron capture center and V_O in both Al_2O_3 and CAAC-IGZO is the possible electron emission center. To clearly understand the electronic properties of Al_2O_3 and CAAC-IGZO with different defects and charge states during the charge transition process, we calculated the density of states (DOS) of Al_2O_3 and CAAC-IGZO with different defects and charge states, respectively.

Figure 6 shows the DOS and the local charge density of hydrogen interstitial in Al_2O_3 dielectric layer. It is found in Figure 6a that, when the charge state in Al_2O_3 with the defects is +1, the protonated hydrogen forms a hydroxide ion with the oxygen ion, at which there is no sub-state in the bandgap. When H_i^+ captures an electron and forms H_i^0, the hydrogen-oxygen bond will be broken and the hydrogen atom moves to the middle of the aluminum ion, as shown in Figure 6b. In this case, a new sub-state DOS arises and is distributed at 3.2 eV above VBM, which is composed of H orbitals and O orbitals. When H_i^0 captures an electron and forms H_i^-, the aluminum ion moves closer to the H atom. The sub-state DOS distributed at 2.6 eV above VBM, composed of H orbitals and O orbitals, which is 0.6 eV lower than H_i^0.

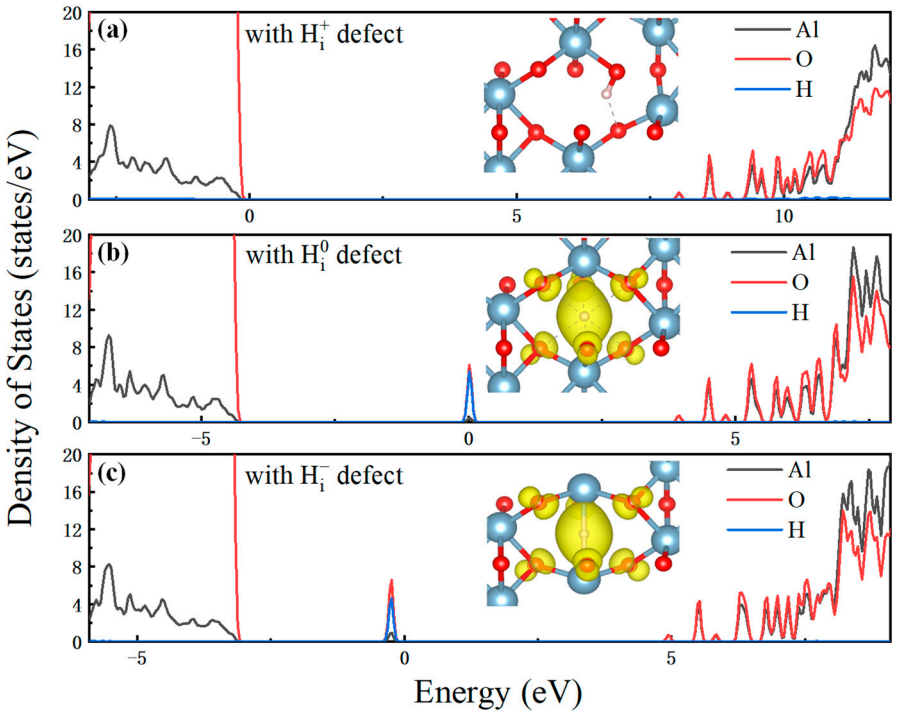

Figure 6. DOS of hydrogen interstitial with the charge states of (**a**) +1, (**b**) 0, and (**c**) −1 in Al_2O_3 dielectric layer, respectively. In inset, the occupied state orbitals are marked by yellow isosurface.

Figure 7 shows the DOS and the local charge density of oxygen vacancies in Al_2O_3 dielectric layer. One can see that, when the defects are in the charge state of 0, the electrons are mainly present in the oxygen vacancies. The sub-state DOS distributes at 2.7 eV above VBM, which is composed of Al orbitals and O orbitals. When V_O^0 emits an electron and forms V_O^+, the aluminium ion moves slightly outward from the oxygen vacancy. The sub-state DOS distributes at 4.1 eV above VBM, which is 0.9 eV higher than V_O^0, as shown in Figure 7b. On the other hand, the electron emission process for the oxygen vacancy from V_O^+ to V_O^{2+} is very similar to that from V_O^0 to V_O^+ process, again with the aluminum ion moves slightly outward from the oxygen vacancy. The sub-state DOS distributes at 5.4 eV above VBM, which is 1.1 eV higher than V_O^+.

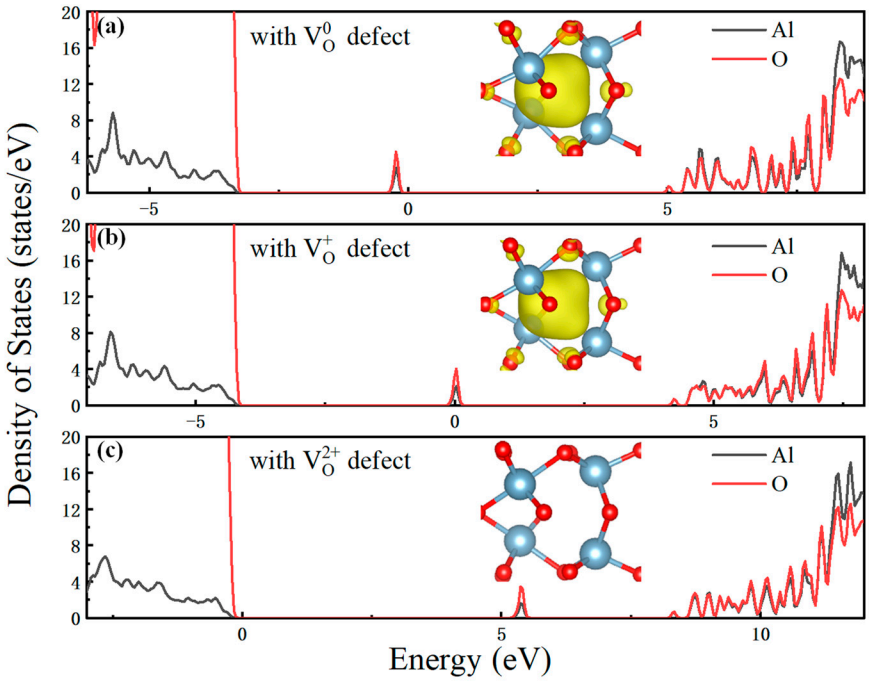

Figure 7. DOS of oxygen vacancy with the charge states of (**a**) 0, (**b**) +1, and (**c**) +2 in Al_2O_3 dielectric layer, respectively. In the inset, the occupied state orbitals are marked by yellow isosurface.

Figure 8 shows the DOS and the local charge density of oxygen vacancies in the CAAC-IGZO active layer. As can be seen in Figure 8 that the electronic properties of four kinds of oxygen vacancies are similar. When the defects are in the charge state of 0, the electrons are mainly present in the oxygen vacancies. The sub-state DOS distributes at 1.6 eV above VBM. For the oxygen vacancies from V_{O1} and V_{O2}, the sub-state DOS is mainly composed of In orbitals and O orbitals, while for V_{O3} and V_{O4}, the sub-state DOS is composed of both Ga orbitals, Zn orbitals and O orbitals. When V_O^0 emits an electron and forms V_O^+, the metal ions move outward from the oxygen vacancy. The sub-state DOS distributes at about 2 eV above VBM, which is 0.4 eV higher than V_O^0. Similarly, the electron emission process for the oxygen vacancies from V_O^+ to V_O^{2+} also arises with the outward movement of metal ions. The sub-state DOS is distributed near the Conduction Band Minimum (CBM).

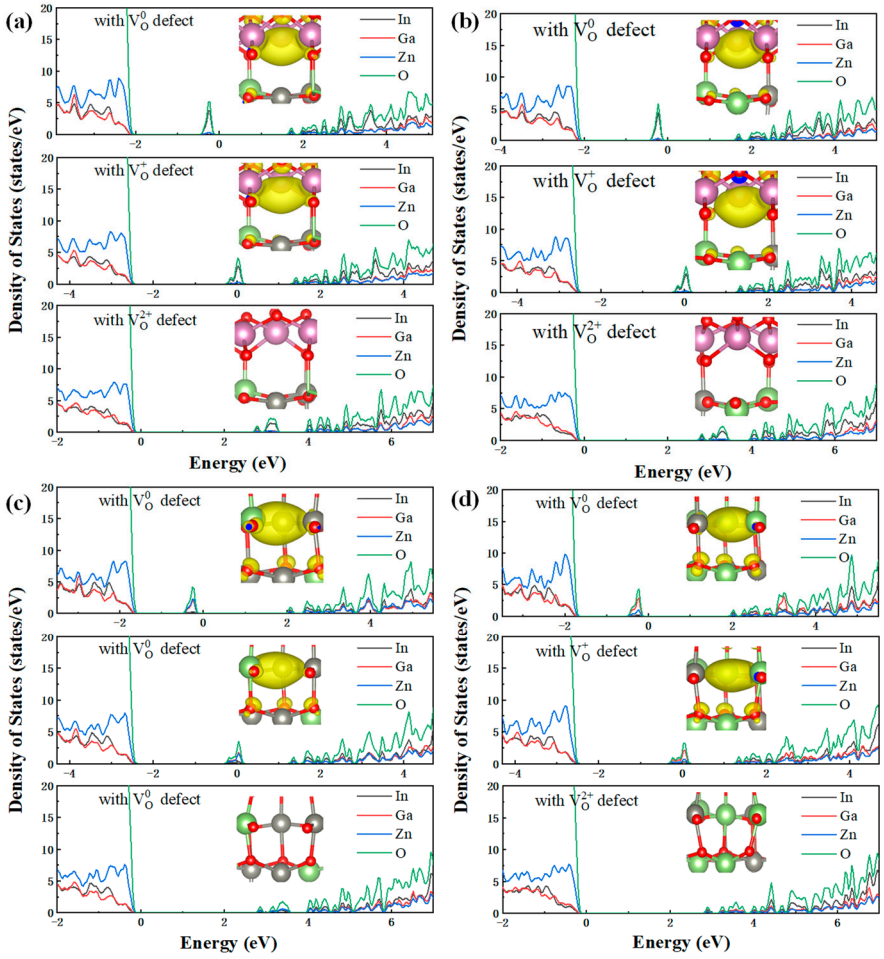

Figure 8. DOS of oxygen vacancy (**a**) V_{O1}, (**b**) V_{O2}, (**c**) V_{O3} and (**d**) V_{O4} with different charge states in CAAC-IGZO active layer.

3.3. Kinetics of Charge Capture/Emission Process

To uncover the kinetics of the charge capture/emission process in CAAC-IGZO FETs, it is crucial to know the activation barrier of the transition process. However, the transition level mentioned above only considers the equilibrium energy relationship between the two-defect charge states and ignores the deformation of the defect site when the charge state is changing. Physically, changes in defect configuration and electron-phonon coupling alter the activation barrier of the charge capture/emission process and will significantly influence the kinetics of the charge capture/emission process. In order to better understand the kinetics of the charge capture/emission process, it is essential to further consider the relationship between the defect formation energy and configuration. The theoretical model used in this work is called as nonradiative multiphonon theory (NMP) [42,43], which has been proven to correctly describe the charge trapping of oxide defects in transistors [44].

3.3.1. Nonradiative Multiphonon Transition Process

Generally, if a defect is neutral in state V_1 and negatively charged in state V_2, the atomic equilibrium configuration is different in each state. Here, the different states are denoted by e_1 and e_2. Since the real motion of atoms is highly complex, one usually uses a single reaction coordinate e to hold all 3N coordinates of the N atoms under consideration. The total energy consists of contributions from the ionic system, the electronic system, and a coupling term in each state. The coupling term describes the shift in the equilibrium positions and the change of the vibrational frequencies. In most case, the energy-

coordinate relationship can be approximated as a quadratic function for small displacement. This simplification can reasonably reflect the essence of the capture process [45]. Another simplification is first-order approximation [45,46], which assumes that only one vibrational mode contributes to the electronic transition process. Based on these approximations, the relationship of total energy to reaction coordinates is usually written as [44],

$$E_{V_i} = \frac{1}{2} M \omega_i^2 (e - e_i)^2 + E_i, \quad (2)$$

where e is the reaction coordinate with the local equilibrium position e_i, M is the effective mass of the 'defect molecule' [47], ω_i is the vibrational frequency of mode i and E_i represent the potential energy of states.

In terms of the relationship of energy to reaction coordinates in Equation (2), one can obtain the relationship of a nonradiative multiphonon transition process, as shown in Figure 9a. In the regular operation of the transistor, photons are not available, which means the increase of energy should only rely on many phonons during the transition process. In Figure 9a, E_{12} and E_{21} are the electron capture and emission energy barriers, respectively. λ_{12} and λ_{21} are the reorganization energies that reflects the strength of electron-phonon coupling, respectively. When an electric field is present at the location of the defect, the total energy difference between two states changes from $E_2 - E_1$ to $E_2' - E_1'$ by qV_{ox}. For defects in the gate dielectric Al_2O_3, V_{ox} is the potential difference at the defect from the interface. For defects in IGZO channel, V_{ox} is the surface potential at the location of defects. Besides, the capture energy barrier and emission energy barrier also change to E_{12}' and E_{21}', as shown in Figure 9b. Then, the rates of transition between two states can be given [44],

$$\begin{cases} k_{12} = N_c v_{th} \sigma e^{-E_{12}/kT} \\ k_{21} = n v_{th} \sigma e^{-E_{21}/kT} \end{cases}, \quad (3)$$

here, N_c is the effective DOS in CBM, n is the electron density of active channel, v_{th} is the thermal velocity of the electron, σ is the capture cross-section, k is the Boltzmann constant, and T is the absolute temperature. According to Equation (3), the effective capture/emission times and the probability of two states occupying at the moment with the infinity of t are given,

$$\begin{cases} \tau_c = \frac{1}{k_{12}} = \tau_0 e^{E_{12}/kT} \\ \tau_e = \frac{1}{k_{21}} = \frac{N_c}{n} \tau_0 e^{E_{21}/kT} \\ P_2 = \frac{k_{12}}{k_{12}+k_{21}} = \frac{1}{1+\frac{n}{N_c} e^{\frac{E_2 - E_1}{kT}}} \\ P_1 = \frac{k_{21}}{k_{12}+k_{21}} = \frac{1}{1+\frac{N_c}{n} e^{\frac{E_1 - E_2}{kT}}} \end{cases}, \quad (4)$$

here, effective time constant τ_0 incorporates the N_c, v_{th} and σ, and is weakly dependent on bias and temperature [48].

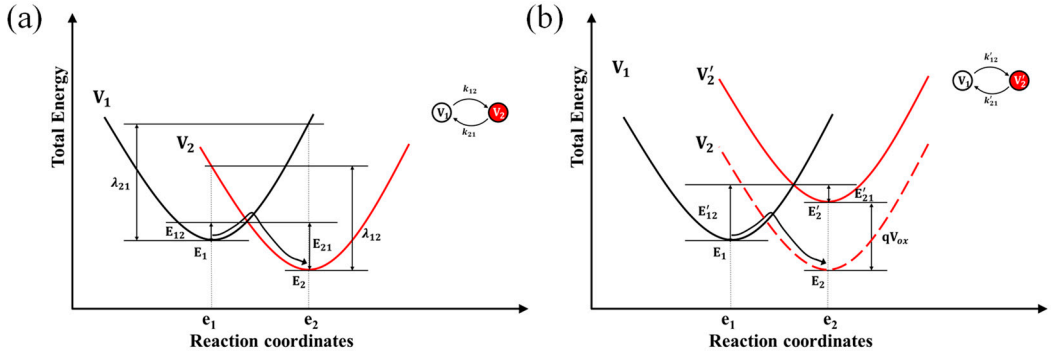

Figure 9. Relationship of total energy to reaction coordinate of nonradiative multiphonon transition process without electric field (**a**) and with an electric field (**b**). V_1 and V_2 represent the neutral state and negative charge state of the defect, respectively. V_2' represents the negative charge state of defect when an electric field is present. E_{12} is the electron capture energy barrier, and E_{21} is the electron emission energy barrier. The vibrational energy of the system is modeled by E_{12} and E_{21}.

Then, the relationship of total energy to coordinates is estimated by using a DFT method. The energy expression of charged state V_1 and charged state V_2 can be expressed as,

$$\begin{cases} E_{V_1}(e) = \frac{1}{2}M\omega_1^2(e-e_1)^2 \\ E_{V_2}(e) = \frac{1}{2}M\omega_2^2(e-e_2)^2 + E_s \\ E_{V_2'}(e) = E_{V_2}(e) - qV_{ox} \\ E_s = E_{V_2}(e_2) - E_{V_1}(e_1) \end{cases}, \quad (5)$$

here, $E_{V_2}(e_1)$ and $E_{V_1}(e_2)$ can be also calculated to define the quadratic function. The coefficient $\frac{1}{2}M\omega_i^2$ can be extracted from the parabolic potential energies.

3.3.2. Charge Transition Process in Al_2O_3

By analyzing the nonradiative multiphonon process, one can discuss the kinetics of the charge transition process. Next, the interstitial hydrogen defect in Al_2O_3 gate dielectric will be discussed, which is a possible electron capture center under PBS in terms of the calculation of the transition levels. Since the capture of electrons by defects has a certain time constant, the probability of a defect capturing two electrons at the same time is very low. Firstly, the charge capture processes from H_i^+ to H_i^0 and H_i^0 to H_i^- will be analyzed, respectively.

Figure 10 shows the total energy as a function of the reaction coordinates for the hydrogen interstitial in the Al_2O_3 dielectric layer and the energy barrier of the transition process. As can be seen in Figure 10a,b that for the transition process from H_i^+ to H_i^0, the reorganization energy λ_{21} required is very high based on the method in Figure 9, reaching to 3.42 eV. The high reorganization energy indicates that the system has a strong electron-phonon coupling in this capture process. Otherwise, combined with the DOS's results in Figure 6, it is found that the vibrational mode of the hydrogen-oxygen bond contributes to this electron capture process. Since the H_i^0 state has a higher equilibrium energy, the capture barrier will become relatively high, reaching to ~1.8 eV. According to Equation (5), this barrier will result in a low capture rate k_{12}. As V_{ox} increases from 0V to 2V, the capture barrier decreases linearly from 1.8 eV to 0.3 eV. Then the capture rate will increase exponentially. For the transition process from H_i^0 to H_i^- in Figure 10c,d that, the reorganization energy λ_{21} is obviously different from that from H_i^+ to H_i^0. The different reorganization energy indicates that the vibrational modes contribute differently to the electronic transition process in the two processes. According to the DOS's results, one can find that the vibrational mode of the adjacent aluminum ion around the hydrogen interstitial contributes to the H_i^0 to H_i^- process, which is different for the process from H_i^+ to H_i^0. At the same time, although the equilibrium energy $E_{H_i^-} - E_{H_i^0}$ decreases continuously, while the probability of defects in H_i^- state increases significantly, according to Equation (5). The capture barrier is basically equal to 0 eV, which means that the electron capture time τ_c from H_i^0 to H_i^- is basically equal to τ_0.

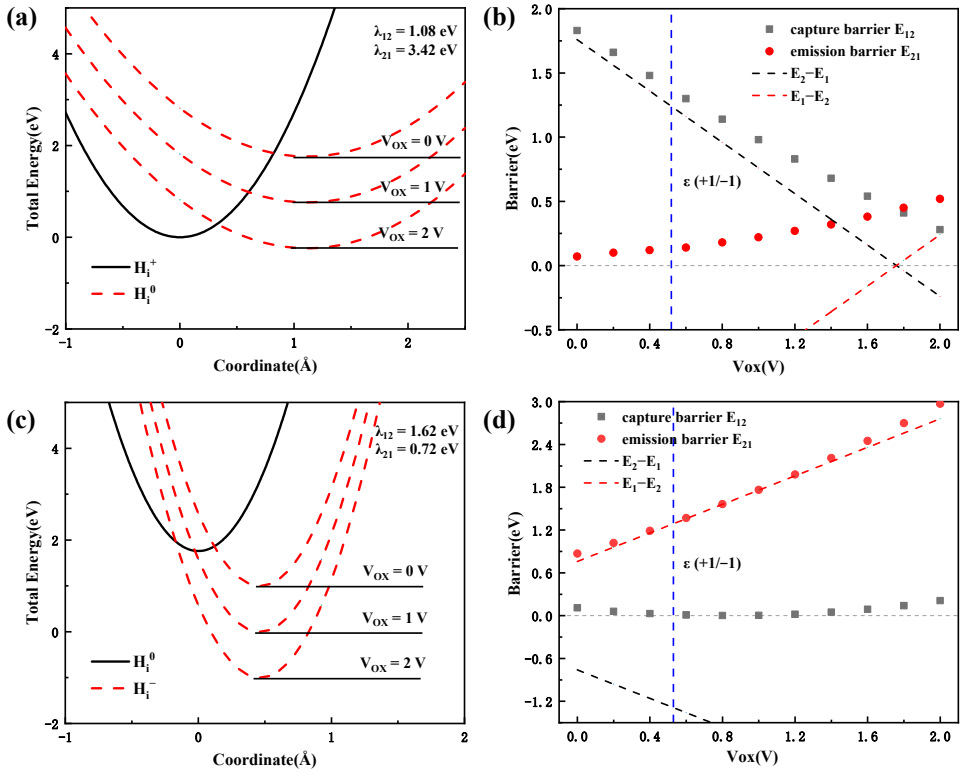

Figure 10. The total energy as a function of the reaction coordinate for the hydrogen interstitial in Al_2O_3 dielectric layer, (**a**) from H_i^+ to H_i^0 and (**c**) from H_i^0 to H_i^-. The energy barrier as a function of V_{ox}, (**b**) from H_i^+ to H_i^0 and (**d**) from H_i^0 to H_i^- process. The red dashed line is the total energy curve for the charge state at different V_{ox}. The blue dash line represent the transition level ε (+1/−1).

Overall, for the H_i^+ defect in the Al_2O_3 gate dielectric, when V_{ox} is greater than 0.52 V, the Fermi level is higher than the transition level ε (+1/−1), and the equilibrium energy of H_i^- is lower than H_i^+, which means that the probability of defects in the state of −1 is higher than that in the state of +1. The electron capture of defects is a favorable energy process. However, the capture barrier is very high (about 1.4 eV), which makes the capture rate of H_i^+ to be very slow. After the electron capture is happened and H_i^0 is formed, the defect will generate electron capture again quickly by a capture time τ_0 and forms H_i^-. As V_{ox} is continuously increased, the capture time τ_c from H_i^+ to H_i^0 will decline exponentially. These kinetic properties suggest that the electron capture process of hydrogen interstitial in Al_2O_3 is relatively slow at low voltage, but rapidly increases at high voltage, and eventually form the negative charge center in the gate dielectric oxide.

Next, we will discuss the transition process of oxygen vacancjes in the Al_2O_3 gate dielectric, which is a possible electron emission center under NBS based on the transition levels mentioned above. Similarly, we analyzed the emission process from V_O^0 to V_O^+ and from V_O^+ to V_O^{2+}, respectively. Figure 11 shows the total energy as a function of the reaction coordinate for the oxygen vacancies in the Al_2O_3 dielectric layer and the energy barrier of the transition process. As can be seen in Figure 11a,c that, for the two transition processes, the reorganization energies are relatively close, suggesting that the vibrational modes contribute to the electronic transition process, which may be the same in both processes. Combining with the DOS's results, one can obtain that the vibrational modes of the adjacent aluminum ion around oxygen vacancies contribute to the electron emission process. According to Figure 11b, for the transition process from V_O^0 to V_O^+, the emission barrier decreases from 1.0 eV to 0 eV as V_{ox} increases from 0 V to 2 V. In Figure 11d, for the transition process from V_O^+ to V_O^{2+}, the emission barrier decreases from 0.5 eV to 0 eV as V_{ox} increases. And as V_{ox} is greater than 1.4 V, the emission barrier increases slightly.

Overall, for V_O^0 defect in the Al_2O_3 gate dielectric, when $|V_{ox}|$ is greater than 0.69 V, the Fermi level is below the transition level ε (+2/−0). Thus, the defects undergo electron emission as an energy favorable process. At this point the emission barrier for the V_O^0 to V_O^+ is about 0.5 eV. Subsequently, V_O^+ then emits an electron again with a much lower emission barrier of about 0.2 eV and forms V_O^{2+}, which represents a significantly lower emission time τ_e for the process from V_O^+ to V_O^{2+}. As $|V_{ox}|$ increases further, the emission time τ_e for the transition process from V_O^0 to V_O^+ decreases rapidly due to a further decrease in the emission barrier, while the emission time τ_e for the transition process from V_O^+ to V_O^{2+} gradually converges to τ_0 and begins to increase as V_{ox} is greater than 1.4 V. As a result, these kinetic properties suggest that the rate of electron emission process from the oxygen vacancies in Al_2O_3 increases as the voltage increases, and finally forms the positive charge center in the gate dielectric oxide.

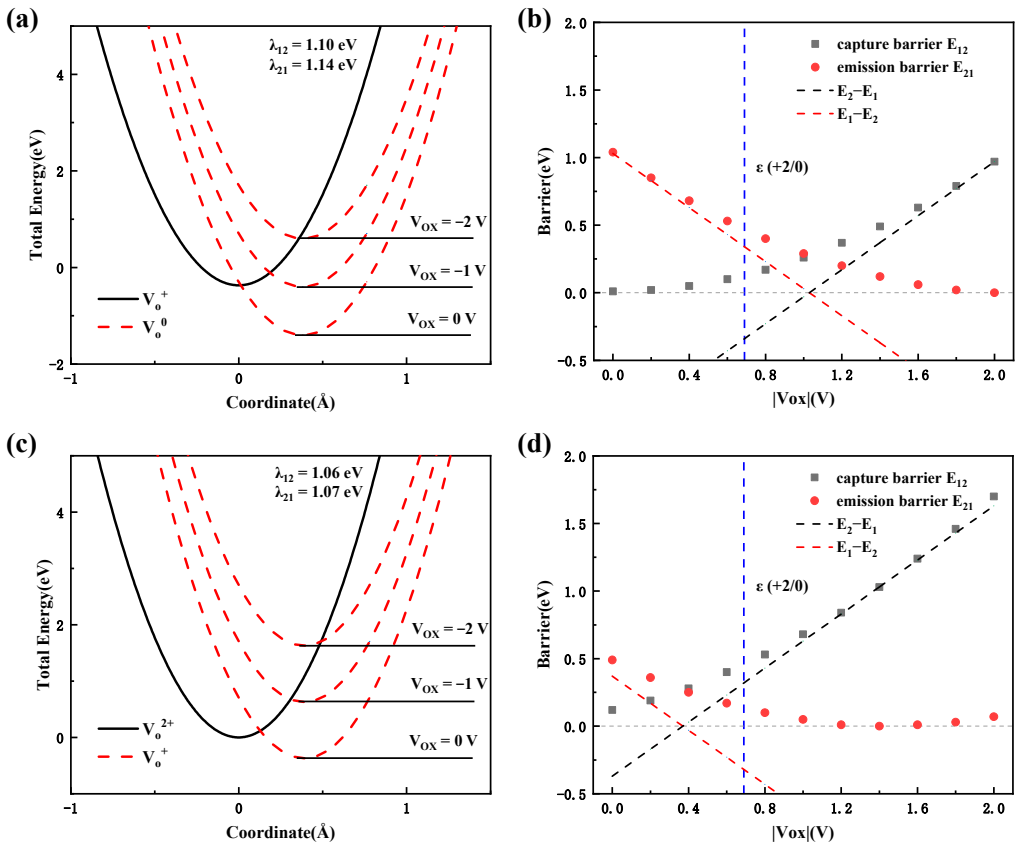

Figure 11. The total energy as a function of reaction coordinates for the oxygen vacancies in Al_2O_3 dielectric layer, (**a**) from V_O^0 to V_O^+ and (**c**) from V_O^+ to V_O^{2+}. The red dashed line is the total energy curve for the charge state at different V_{ox}. The energy barrier as a function of V_{ox}, (**b**) from V_O^0 to V_O^+ and (**d**) from V_O^+ to V_O^{2+}. The blue dash line represent the transition level ε (+2/0).

3.3.3. Charge Transition Process in CAAC-IGZO

Finally, we will discuss the electron emission process of the oxygen vacancies in the CAAC-IGZO active layer. Figure 12 shows the total energy as a function of the reaction coordinate for the oxygen vacancies in the CAAC-IGZO active layer and the energy barrier of the transition process, respectively. Based on the results mentioned above, four kinds of oxygen vacancies in CAAC-IGZO are similar. Here, we only discuss the transition process of V_{O2}. As can be seen in Figure 12a,c that, for the electron emission processes from V_O^0 to V_O^+ and from V_O^+ to V_O^{2+}, the reorganization energies are very close. The results imply that the vibrational modes contribute to the electronic emission process, which may be the same in both processes. The DOS's results also display that the vibrational

modes of the adjacent metal ion around oxygen vacancy contribute to the electron emission process. The lower reorganization energy represents a weaker electron-phonon coupling of the oxygen vacancies in the CAAC-IGZO active layer, as compared with the defect transition process in Al_2O_3. In Figure 12b, one can see that for the transition process from V_O^0 to V_O^+, the emission barrier decreases rapidly from 1.0 eV to 0 eV as $|V_{ox}|$ increases slightly at $|V_{ox}|$ being greater than 1.6 V. In Figure 12d, for the transition process from V_O^+ to V_O^{2+}, the emission barrier decreases from 0.6 eV to 0 eV as $|V_{ox}|$ increases and begins to increase when $|V_{ox}|$ is greater than 1.2 V. The emission barrier is approximately 0.2 eV, as $|V_{ox}|$ is equal to 2 V.

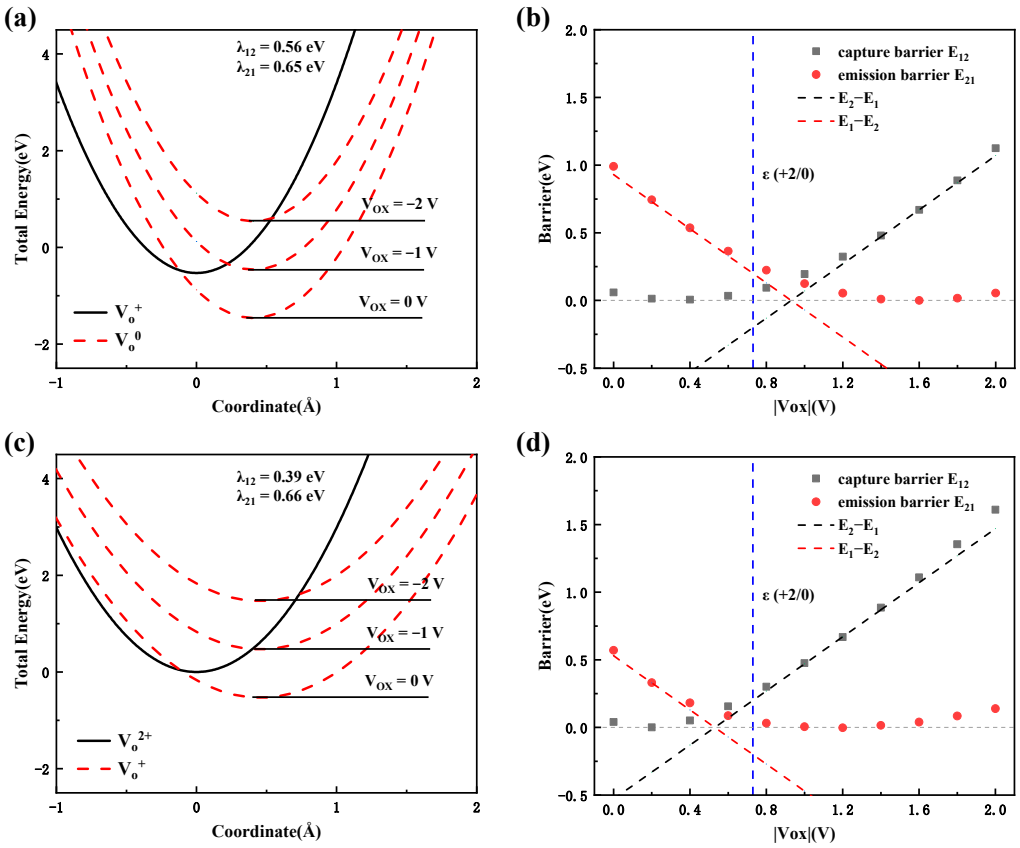

Figure 12. The total energy as a function of reaction coordinates for the oxygen vacancies in CAAC-IGZO active layer, (**a**) from V_O^0 to V_O^+ and (**c**) from V_O^+ to V_O^{2+}. The red dashed line is the total energy curve for the charge state at different V_{ox}. The energy barrier as a function of V_{ox}, (**b**) from V_O^0 to V_O^+ and (**d**) from V_O^+ to V_O^{2+}. The blue dash line represent the transition level ε (+2/0).

Overall, for the V_O^0 defect in the CAAC-IGZO active layer, when V_{ox} is greater than 0.73 V. the Fermi level is below the transition energy level ε (+2/−0), the defects undergo the electron emission as a favorable energy process. At that point, the emission barrier for the transition process from V_O^0 to V_O^+ is about 0.25 eV. Subsequently, the V_O^+ defect is then emitted again with a much lower emission energy of about 0.1 eV. As $|V_{ox}|$ increases further, the emission time τ_e for the transition process from V_O^0 to V_O^+ decreases rapidly to τ_0 and begins to increase at $|V_{ox}|$ greater than 1.6 V, while the emission time τ_e for the transition process from V_O^+ to V_O^{2+} converges to τ_0 and begins to increase at $|V_{ox}|$ greater than 1.2 V. These kinetics properties suggest that the rate of the electron emission process increases with the increasing voltage, then begins to slow down when the voltage reaches about 1.6V, and finally forming a positive charge center in the active layer.

3.4. Instability Effects in IGZO Device Induced by Charge Capture/emission Process

As mentioned above, the instability of the CAAC-IGZO FETs is mainly reflected in the drift of the threshold voltage under NBS and PBS. To uncover the instability, we then discuss the instability effects in IGZO devices induced by the charge capture/emission process. General speaking, the change of defect charge state caused by the charge capture/emission process will leave a new positive or negative charge center in oxide semiconductors and gate dielectric, which can be observed macroscopically as a change of fixed oxide charge per area (Q_{ox}) and affects the electrical performance of the device. The relationship of the threshold voltage drifts with Q_{ox} is described as [44],

$$\Delta V_{th}(V_G) = -\frac{\Delta Q_{ox}(V_G)}{C_{ox}}, \quad (6)$$

here, C_{ox} is the capacitance per area of gate dielectric. Universally, the capture/emission process of the oxygen vacancies does not quickly follow the gate bias change, which will be experimental recorded as a BTI effects. Under PBS, the electron capture process of hydrogen interstitial in the Al_2O_3 dielectric layer will decrease the value of Q_{ox}, and then induce a positive drift of the threshold voltage. In a 2T0C DRAM cell, this PBS-induced positive drift occurs within the write transistor and read transistor of the write operation and results in lower open-state current and slower write operations. In addition, the large capture barrier and capture time of the process from H_i^+ to H_i^0 will cause a small drift of the threshold voltage at lower temperatures and low positive gate bias voltage. The experiment displays that the Al_2O_3 gate dielectric with 1.1% hydrogen concentration may result in a positive but small ΔV_{th} at 25 °C under PBS [33]. While the trap level E_t tested by IPE measurements is 0.69 eV above the Fermi level, which is similar to our results. However, the ΔV_{th} will become negative as the temperature raising. The reason is that under higher stress, trapped hydrogen in the gate-dielectric is released, diffuses to IGZO layer. To overcome the instability, some approaches can be taken to control the hydrogen concentration in Al_2O_3 dielectric layer, such as replacing water with ozone as a precursor for ALD of the gate dielectric.

Under NBS, the electron emission process of the oxygen vacancies in the Al_2O_3 dielectric layer and CAAC-IGZO active layer will lead to the increase of Q_{ox}, and then induce a negative drift of the threshold voltage. In a 2T0C DRAM cell, the NBS-induced negative drift occurs within the write transistor of the read operation and results in larger off-state current and shorter retention time. Generally, the transistor is in off-state under a negative gate bias. The phenomenon of the negative drift of the threshold voltage will be observed when transistor is in on-state again and one can find a hysteresis of the current-voltage curve. To better understand the phenomenon of the negative drift of the threshold voltage induced, one firstly need to distinguish between the different contributions of the oxygen vacancies in the Al_2O_3 dielectric layer and CAAC-IGZO active layer to the threshold voltage drift, respectively. According to the calculations, the behavior of the oxygen vacancies in the Al_2O_3 dielectric layer and CAAC-IGZO active layer is essentially similar. However, it should be noted, that V_{ox} is the surface potential at the defect for the active layer and the potential difference at the defect for the dielectric layer. It is well known that when the gate bias of transistor is below the threshold voltage, more voltage will fall on the active layer thus changing the surface potential and the carrier concentration. Therefore, the oxygen vacancies in CAAC-IGZO active layer may contribute more to the negative drift of the threshold. The effect of the oxygen vacancies under NBS is very similar to that in amorphous IGZO [31], except that the oxygen vacancies in CAAC-IGZO do not lead to the formation of shallow donors. To overcome the instability, some approaches can be taken to control the concentration of the oxygen vacancy, such as annealing in an oxygen atmosphere.

4. Conclusions

In this work, the charge capture and emission properties of different defects in the CAAC-IGZO FETs have been studied by using the first-principles calculations. The results

display that the hydrogen interstitials in the Al_2O_3 dielectric layer are probable electron emission center, as well as the oxygen vacancies in Al_2O_3 dielectric layer and CAAC-IGZO active layer as the electron emission center. More importantly, by combining the nonradiative multiphonon theory, we discussed the configuration change and kinetics of different transition processes in detail. It is found that a high capture barrier about 1.4 eV for electron capture process of hydrogen interstitial in Al_2O_3 dielectric layer and an emission barrier of about 0.5 eV and 0.25 eV for the electron emission process of the oxygen vacancies in Al_2O_3 dielectric layer and CAAC-IGZO active layer, can be formed, respectively. The formation of these charge centers will seriously affect the charge capture/emission process and then induce the instability of the CAAC-IGZO FETs, where hydrogen interstitials cause a positive drift of the threshold voltage and oxygen vacancies cause a negative drift of the threshold voltage. This work helps understand the mechanisms of instability of CAAC-IGZO transistor caused by carrier capture/emission process and provides a theoretical reference for the improvement of the experiment.

Author Contributions: Z.W., software, investigation, data curation, writing—original draft preparation, methodology. N.L., validation, writing—review and editing, supervision, project administration. J.W., supervision, methodology. D.G., validation, supervision. L.W., software, methodology. G.Y., writing—review and editing. All authors have read and agreed to the published version of the manuscript.

Funding: This work was funded by (a) the National key research and development program (Grant Nos. 2018YFA0208503, 2022YFB3606902), (b) the National Natural Science Foundation of China (Grant Nos. 61890944, 61888102, 92264204, 62274178,61720106013, 61904195, and 62004214), (c) the Strategic Priority Research Program of Chinese Academy of Sciences (Grant No. XDB30030000, XDB30030300).

Institutional Review Board Statement: Not applicable.

Informed Consent Statement: Not applicable.

Data Availability Statement: All data used in this work will be available upon reasonable request.

Acknowledgments: This work was supported in part by the National key research and development program (Grant Nos. 2018YFA0208503, 2022YFB3606902), by the Opening Project of Key Laboratory of Microelectronic Devices and Integrated Technology, Institute of Microelectronics, Chinese Academy of Sciences, and by the National Natural Science Foundation of China (Grant Nos. 61890944, 61888102, 92264204, 62274178, 61720106013, 61904195, and 62004214), by the Strategic Priority Research Program of Chinese Academy of Sciences (Grant No. XDB30030000, XDB30030300).

Conflicts of Interest: The authors declare no conflict of interest.

References

1. Nomura, K.; Ohta, H.; Takagi, A.; Kamiya, T.; Hirano, M.; Hosono, H. Room-temperature fabrication of transparent flexible thin-film transistors using amorphous oxide semiconductors. *Nature* **2004**, *432*, 488–492. https://doi.org/10.1038/nature03090.
2. Kamiya, T.; Nomura, K.; Hosono, H. Present status of amorphous In-Ga-Zn-O thin-film transistors. *Sci. Technol. Adv. Mater.* **2010**, *11*, 044305. https://doi.org/10.1088/1468-6996/11/4/044305.
3. Wager, J.F.; Yeh, B.; Hoffman, R.L.; Keszler, D.A. An amorphous oxide semiconductor thin-film transistor route to oxide electronics. *Curr. Opin. Solid State Mater. Sci.* **2014**, *18*, 53–61. https://doi.org/10.1016/j.cossms.2013.07.002.
4. Jeong, J.K. The status and perspectives of metal oxide thin-film transistors for active matrix flexible displays. *Semicond. Sci. Technol.* **2011**, *26*, 034008. https://doi.org/10.1088/0268-1242/26/3/034008.
5. Hsu, C.M.; Tzou, W.C.; Yang, C.F.; Liou, Y.J. Investigation of the High Mobility IGZO Thin Films by Using Co-Sputtering Method. *Materials* **2015**, *8*, 2769–2781. https://doi.org/10.3390/ma8052769.
6. Kato, K.; Shionoiri, Y.; Sekine, Y.; Furutani, K.; Hatano, T.; Aoki, T.; Sasaki, M.; Tomatsu, H.; Koyama, J.; Yamazaki, S. Evaluation of Off-State Current Characteristics of Transistor Using Oxide Semiconductor Material, Indium-Gallium-Zinc Oxide. *Jpn. J. Appl. Phys.* **2012**, *51*, 021201. https://doi.org/10.1143/jjap.51.021201.
7. Oota, M.; Ando, Y.; Tsuda, K.; Koshida, T.; Oshita, S.; Suzuki, A.; Fukushima, K.; Nagatsuka, S.; Onuki, T.; Hodo, R.; et al. 3D-Stacked CAAC-In-Ga-Zn Oxide FETs with Gate Length of 72 nm. In Proceedings of the 65th IEEE Annual International Electron Devices Meeting (IEDM), San Francisco, CA, USA, 9–11 December 2019.

8. Kunitake, H.; Ohshima, K.; Tsuda, K.; Matsumoto, N.; Sawai, H.; Yanagisawa, Y.; Saga, S.; Arasawa, R.; Seki, T.; Tokumaru, R.; et al. High thermal tolerance of 25-nm c-axis aligned crystalline In-Ga-Zn oxide FET. In Proceedings of the 64th IEEE Annual International Electron Devices Meeting (IEDM), San Francisco, CA, USA, 1–5 December 2018.
9. Samanta, S.; Han, K.Z.; Sun, C.; Wang, C.K.; Thean, A.V.Y.; Gong, X.. Amorphous IGZO TFTs featuring Extremely-Scaled Channel Thickness and 38 nm Channel Length: Achieving Record High G(m,max) of 125 μS/μm at V-DS of 1 V and I-ON ( ) of 350 μA/μm. In Proceedings of the IEEE Symposium on VLSI Technology and Circuits, Electr Network, Honolulu, HI, USA, 15–19 June 2020.
10. Sheng, J.; Hong, T.; Lee, H.M.; Kim, K.; Sasase, M.; Kim, J.; Hosono, H.; Park, J.S. Amorphous IGZO TFT with High Mobility of similar to 70 cm(2)/(V s) via Vertical Dimension Control Using PEALD. *ACS Appl. Mater. Interfaces* **2019**, *11*, 40300–40309. https://doi.org/10.1021/acsami.9b14310.
11. Saito, N.; Sawabe, T.; Kataoka, J.; Ueda, T.; Tezuka, T.; Ikeda, K. High mobility (>30 $cm^2V^{-1}s^{-1}$) and low source/drain parasitic resistance In-Zn-O BEOL transistor with ultralow <10–20 A μm^{-1} off-state leakage current. *Jpn. J. Appl. Phys.* **2019**, *58*, SBBJ07. https://doi.org/10.7567/1347-4065/ab01d7.
12. Belmonte, A.; Oh, H.; Rassoul, N.; Donadio, G.L.; Mitard, J.; Dekkers, H.; Delhougne, R.; Subhechha, S.; Chasin, A.; van Setten, M.J.; et al. Capacitor-less, Long-Retention (>400 s) DRAM Cell Paving the Way towards Low-Power and High-Density Monolithic 3D DRAM. In Proceedings of the IEEE International Electron Devices Meeting (IEDM), Electr Network, San Francisco, CA, USA, 12–18 December 2020.
13. Shunpei Yamazaki, M.F. *Physics and Technology of Crystalline Oxide Semiconductor CAAC-IGZO: Application to LSI*; Wiley Publishing: Hoboken, NJ, USA, 2016.
14. Nomura, K.; Kamiya, T.; Kikuchi, Y.; Hirano, M.; Hosono, H. Comprehensive studies on the stabilities of a-In-Ga-Zn-O based thin film transistor by constant current stress. *Thin Solid Films* **2010**, *518*, 3012–3016. https://doi.org/10.1016/j.tsf.2009.09.193.
15. Domen, K.; Miyase, T.; Abe, K.; Hosono, H.; Kamiya, T. Positive Gate Bias Instability Induced by Diffusion of Neutral Hydrogen in Amorphous In-Ga-Zn-O Thin-Film Transistor. *IEEE Electron. Device Lett.* **2014**, *35*, 832–834. https://doi.org/10.1109/led.2014.2327234.
16. Jeong, J.K.; Yang, H.W.; Jeong, J.H.; Mo, Y.G.; Kim, H.D. Origin of threshold voltage instability in indium-gallium-zinc oxide thin film transistors. *Appl. Phys. Lett.* **2008**, *93*, 123508. https://doi.org/10.1063/1.2990657.
17. Cai, M.X.; Yao, R.H. Modeling and characterization of the low frequency noise behavior for amorphous InGaZnO thin film transistors in the subthreshold region. *J. Appl. Phys.* **2017**, *122*, 154503. https://doi.org/10.1063/1.4994152.
18. Kim, K.A.; Park, M.J.; Lee, W.H.; Yoon, S.M. Characterization of negative bias-illumination-stress stability for transparent top-gate In-Ga-Zn-O thin-film transistors with variations in the incorporated oxygen content. *J. Appl. Phys.* **2015**, *118*, 234504. https://doi.org/10.1063/1.4938013.
19. Martins, J.; Bahubalindruni, P.; Rovisco, A.; Kiazadeh, A.; Martins, R.; Fortunato, E.; Barquinha, P. Bias Stress and Temperature Impact on InGaZnO TFTs and Circuits. *Materials* **2017**, *10*, 680. https://doi.org/10.3390/ma10060680.
20. Kresse, G.; Furthmuller, J. Efficient iterative schemes for ab initio total-energy calculations using a plane-wave basis set. *Phys. Rev. B* **1996**, *54*, 11169–11186. https://doi.org/10.1103/PhysRevB.54.11169.
21. Blochl, P.E. Projector Augmented-Wave Method. *Phys. Rev. B* **1994**, *50*, 17953–17979. https://doi.org/10.1103/PhysRevB.50.17953.
22. Perdew, J.P.; Burke, K.; Wang, Y. Generalized gradient approximation for the exchange-correlation hole of a many-electron system. *Phys. Rev. B* **1996**, *54*, 16533–16539. https://doi.org/10.1103/PhysRevB.54.16533.
23. Heyd, J.; Scuseria, G.E.; Ernzerhof, M. Hybrid functionals based on a screened Coulomb potential. *J. Chem. Phys.* **2003**, *118*, 8207–8215. https://doi.org/10.1063/1.1564060.
24. Dudarev, S.L.; Botton, G.A.; Savrasov, S.Y.; Humphreys, C.J.; Sutton, A.P. Electron-energy-loss spectra and the structural stability of nickel oxide: An LSDA+U study. *Phys. Rev. B* **1998**, *57*, 1505–1509. https://doi.org/10.1103/PhysRevB.57.1505.
25. Choi, M.; Janotti, A.; Van de Walle, C.G. Native point defects and dangling bonds in alpha-Al_2O_3. *J. Appl. Phys.* **2013**, *113*, 044501. https://doi.org/10.1063/1.4784114.
26. Damour, H.; Schiferl, D.; Denner, W.; Schulz, H.; Holzapfel, W.B. High-Pressure Single-Crystal Structure Determinations for Ruby up to 90-Kbar Using An Automatic Diffractometer. *J. Appl. Phys.* **1978**, *49*, 4411–4416. https://doi.org/10.1063/1.325494.
27. Kimizuka, N.; Mohri, T. Spinel, $YbFe_2O_4$, And $Yb_2Fe_3O_7$ Types of Structures for Compounds in the In_2O_3 And Sc_2O_3-A_2O_3-Bo Systems A-Fe, Ga, Or Al-B-Mg, Mn, Fe, Ni, Cu, or Zn at Temperatures over 1000-Degrees-C. *J. Solid State Chem.* **1985**, *60*, 382–384. https://doi.org/10.1016/0022-4596(85)90290-7.
28. Ishihara, N.; Tsubuku, M.; Nonaka, Y.; Watanabe, R.; Inoue, K.; Shishido, H.; Kato, K.; Yamazaki, S.; Japan Soc Appl, P. Optical Properties and Evaluation of Localized Level in Gap of In-Ga-Zn-O Thin Film. In Proceedings of the 19th International Workshop on Active-Matrix Flatpanel Displays and Devices (AM-FPD)—TFT Technologies and FPD Materials, Ryukoku Univ, Kyoto, Japan, 4–6 July 2012; pp. 143–146.
29. Nakashima, M.; Oota, M.; Ishihara, N.; Nonaka, Y.; Hirohashi, T.; Takahashi, M.; Yamazaki, S.; Obonai, T.; Hosaka, Y.; Koezuka, J. Origin of major donor states in In-Ga-Zn oxide. *J. Appl. Phys.* **2014**, *116*, 213703. https://doi.org/10.1063/1.4902859.
30. Scofield, J.H.; Doerr, T.P.; Fleetwood, D.M. Correlation between Preirradiation 1/F Noise and Postirradiation Oxide-Trapped Charge in Mos-Transistors. *IEEE Trans. Nucl. Sci.* **1989**, *36*, 1946–1953. https://doi.org/10.1109/23.45391.
31. de Meux, A.D.; Bhoolokam, A.; Pourtois, G.; Genoe, J.; Heremans, P. Oxygen vacancies effects in a-IGZO: Formation mechanisms, hysteresis, and negative bias stress effects. *Phys. Status Solidi A-Appl. Mater. Sci.* **2017**, *214*, 1600889. https://doi.org/10.1002/pssa.201600889.

32. Korner, W.; Urban, D.F.; Elsasser, C. Origin of subgap states in amorphous In-Ga-Zn-O. *J. Appl. Phys.* **2013**, *114*, 163704. https://doi.org/10.1063/1.4826895.
33. Chasin, A.; Franco, J.; Triantopoulos, K.; Dekkers, H.; Rassoul, N.; Belmonte, A.; Smets, Q.; Subhechha, S.; Claes, D.; van Setten, M.J.; et al. Understanding and modelling the PBTI reliability of thin-film IGZO transistors. In Proceedings of the IEEE International Electron Devices Meeting (IEDM), San Francisco, CA, USA, 11–16 December 2021.
34. Velichko, R.; Magari, Y.; Furuta, M. Defect Passivation and Carrier Reduction Mechanisms in Hydrogen-Doped In-Ga-Zn-O (IGZO:H) Films upon Low-Temperature Annealing for Flexible Device Applications. *Materials* **2022**, *15*, 334. https://doi.org/10.3390/ma15010334.
35. Fan, C.L.; Shang, M.C.; Li, B.J.; Lin, Y.Z.; Wang, S.J.; Lee, W.D.; Hung, B.R. Teflon/SiO_2 Bilayer Passivation for Improving the Electrical Reliability of Oxide TFTs Fabricated Using a New Two-Photomask Self-Alignment Process. *Materials* **2015**, *8*, 1704–1713. https://doi.org/10.3390/ma8041704.
36. Momma, K.; Izumi, F. VESTA: A three-dimensional visualization system for electronic and structural analysis. *J. Appl. Crystallogr.* **2008**, *41*, 653–658. https://doi.org/10.1107/s0021889808012016.
37. Van de Walle, C.G.; Neugebauer, J. First-principles calculations for defects and impurities: Applications to III-nitrides. *J. Appl. Phys.* **2004**, *95*, 3851–3879. https://doi.org/10.1063/1.1682673.
38. Zhang, S.B.; Northrup, J.E. Chemical-Potential Dependence of Defect Formation Energies in Gaas—Application to Ga Self-Diffusion. *Phys. Rev. Lett.* **1991**, *67*, 2339–2342. https://doi.org/10.1103/PhysRevLett.67.2339.
39. Wei, S.H. Overcoming the doping bottleneck in semiconductors. *Comput. Mater. Sci.* **2004**, *30*, 337–348. https://doi.org/10.1016/j.commatsci.2004.02.024.
40. Kamiya, T.; Nomura, K.; Hosono, H. Origins of High Mobility and Low Operation Voltage of Amorphous Oxide TFTs: Electronic Structure, Electron Transport, Defects and Doping. *J. Disp. Technol.* **2009**, *5*, 273–288. https://doi.org/10.1109/jdt.2009.2021582.
41. Zaki, S.E.; Basyooni, M.A.; Shaban, M.; Rabia, M.; Eker, Y.R.; Attia, G.F.; Yilmaz, M.; Ahmed, A.M. Role of oxygen vacancies in vanadium oxide and oxygen functional groups in graphene oxide for room temperature CO_2 gas sensors. *Sens. Actuators A-Phys.* **2019**, *294*, 17–24. https://doi.org/10.1016/j.sna.2019.04.037.
42. Henry, C.H.; Lang, D.V. Nonradiative Capture and Recombination by Multiphonon Emission in Gaas and Gap. *Phys. Rev. B* **1977**, *15*, 989–1016. https://doi.org/10.1103/PhysRevB.15.989.
43. Makramebeid, S.; Lannoo, M. Quantum Model for Phonon-Assisted Tunnel Ionization of Deep Levels in A Semiconductor. *Phys. Rev. B* **1982**, *25*, 6406–6424. https://doi.org/10.1103/PhysRevB.25.6406.
44. Grasser, T. Stochastic charge trapping in oxides: From random telegraph noise to bias temperature instabilities. *Microelectron. Reliab.* **2012**, *52*, 39–70. https://doi.org/10.1016/j.microrel.2011.09.002.
45. Stoneham, A.M. Nonradiative-Transitions in Semiconductors. *Rep. Prog. Phys.* **1981**, *44*, 1251–1295. https://doi.org/10.1088/0034-4885/44/12/001.
46. Schenk, A.; Enderlein, R.; Suisky, D. Field-Dependent Emission Rate at Deep Centers in GAAS by Using a 2-Phonon Mode Model. *Acta Phys. Pol. A* **1986**, *69*, 813–816.
47. Schanovsky, F.; Gos, W.; Grasser, T. Multiphonon hole trapping from first principles. *J. Vac. Sci. Technol. B* **2011**, *29*, 01A201. https://doi.org/10.1116/1.3533269.
48. Grasser, T. Bias Temperature Instability for Devices and Circuits. In *The Capture/Emission Time Map Approach to the Bias Temperature Instability*; Grasser, T., Ed.; Springer: New York, NY, USA, 2014; pp. 447–481.